Chapter 5

Numerical modelling of layered two-dimensional photonic structures

The accurate computation of the diffraction properties of zero-order dielectric structures is very much the subject of current scientific research, in connection with a multitude of applications in the fields of telecommunications, and other optics technologies. In recent years, the introduction of photonic crystals (PCs) has added more complexity to the theoretical tasks in diffractive optics by generating the need to compute the diffraction of layered diffractive structures, which requires the computation of electromagnetic fields penetrating deeply into complex dielectric structures.

With the aim of understanding the mechanisms behind the phenomenology in the production of structural colour on the wings of some species of butterflies, the models used to compute the optical response of microstructured butterfly scales has become increasingly complex and some of the computational techniques of diffractive optics have been recently employed.

In this chapter, a method to compute the diffraction of volume diffractive structures is presented, which is based on the use of a finite-difference time-domain (FDTD) algorithm and a numerical near-field to far-field transformation

(NFFFT) algorithm. The theoretical background of this method has been presented in section 2.3 and here numerical issues are discussed in relation to the applications presented thereafter.

Using this method, a study of fundamental morphological features of the microstructure found on the wings of the tropical butterfly *Morpho rhetenor* has been carried out. Additionally, dielectric structures comparable to those occurring in the fabricated devices reported in chapter 3 were numerically investigated.

5.1 Numerical computation: method and issues

To compute diffraction efficiencies, first the *Maxwell*'s equations were solved numerically using the finite-difference time-domain method (FDTD) discussed in section 2.3.1, and successively, a near-field to far-field transformation (NFFFT) was performed on the FDTD solutions as discussed in section 2.3.2. All computations were run on personal computers having 256MB of RAM, they were performed at a 32bit precision and required several hours each, and their duration depended mainly on the speed of the processor and on the size of the computation grid.

The following features characterised the FDTD core algorithm:

- The computations were performed on an orthogonal and uniform grid.
- Fourth-order, staggered polynomial spatial difference schemes were used.
- Time derivatives were calculated with second-order difference schemes.
- The algorithm incorporated absorbing, perfectly matched layer (PML) boundary conditions involving a split-field representation of the electromagnetic fields.
- The initial condition was a wide-front *Gaussian* wavepacket propagating along one of the orthogonal axes of the grid.
- Smoothing of the dielectric was included.

The nodes of the computation grid were $5nm$ ($= \Delta s$) apart and time was stepped in intervals of $4 \cdot 10^{-18}s$ ($=\Delta t$), which yielded stable and accurate solutions in the visible spectrum. The computations for transverse electric (TE) polarised fields (*i.e.* having the electric field oriented perpendicularly to the incidence and simulation plane) and transverse magnetic (TM) polarised

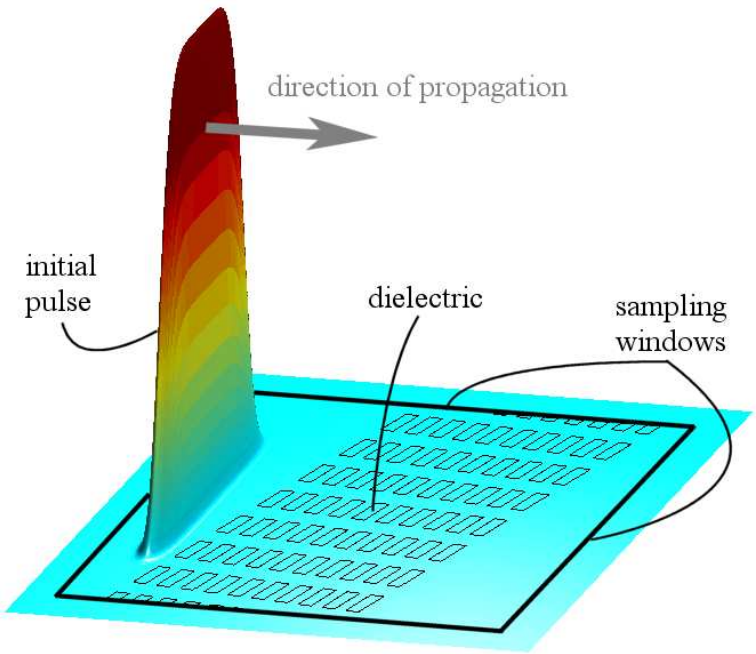

Figure 5.1: Plot of the initial field of a typical computation defined over the entire grid with superimposed contour plot of the dielectric structure and a schematic view of the sampling windows.

ones (*i.e.* having the magnetic field oriented perpendicularly to the incidence and simulation plane) were performed separately.

The use of absorbing boundary conditions with a finite initial pulse, as opposed to periodic boundary conditions and an infinitely wide incident field, allowed one to model the finiteness of the volume in which the interaction between light and the diffractive structures takes place. In conjunction with the experiments discussed in chapter 4, where the incident beam was focussed to a spot with a diameter of few microns, this modelling approach proved particularly useful.

The initial condition was a pulse propagating along one of the grid axes with a *Gaussian* shape in the direction of propagation ($FWHM = 80nm$) and that of a *supergaussian* perpendicularly to it ($FWHM = 2200nm$), which resulted in a wavepacket coherently propagating through the simulation grid. The absorbing PML boundary consisted of 50 grid points surrounding the

computation area. The scattered fields were sampled at points of the grid $500nm$ (100 grid points) away from the edges of the computed zone and the sampling points were chosen along four straight windows resulting in a closed rectangle, the size of which depended on the extension of the computation area.

Figure 5.1 shows the initial condition for a typical computation; the electric field, defined over the entire grid, is depicted together with a superimposed contour plot of the dielectric structure and a schematic view of the sampling windows. A certain degree of dispersion of the wavepacket during propagation, an effect due to the natural spread of *Gaussian* waveforms, resulted in a widening of the initial field edges. Also, the finite width of the pulse generated an intrinsic diffractive behaviour of the initial field, which manifested differently for various lengths of propagation, following the change in pulse width with time. Whereas a wide front pulse propagates more coherently than a narrow, purely *Gaussian* one, it also causes diffraction, and therefore the choice of a suitable width is a compromise between these two properties. To minimise computational artifacts in the sampled diffracted fields, the width of the initial field was optimised in order not to generate any substantial field leaks from the sides of the dielectric structures on one hand, and to propagate coherently on the other. Additionally, the diverging initial pulse, where occurring, was removed from the sampled diffracted fields, thus only allowing for the diffracted field to be sampled. It was not possible however to eliminate the intrinsic diffraction and a certain degree of angular dispersion of the initial pulse, which were transferred into the sampled fields and were, together with numerical diffusion, the major sources of error.

The diffraction for different angles of incidence was computed by changing the orientation of the dielectric with respect to the direction of propagation of the initial wavepacket, which was kept constant. Three angles of incidence were computed for all studied structures for comparison with the experimental data: 10°, 30° and 60°. In order to maintain similar conditions of

incidence and therefore the same width of the initial pulse for all the computed cases, and to ensure accurate computation of the backscattered fields, the size of the computation area was differently chosen for each angle of incidence: a grid with 1200×750 nodes was used for the computations at an angle of incidence of 10°; a 1200×1200 nodes grid for 30°; and a 1200×1800 nodes one for 60°. Rotating the dielectric structure with respect to the initial pulse meant that the field interacted with a larger number of diffractive elements for larger angles of incidence, which resulted in sharper diffraction features. Also, the average distance covered by the initial pulse before entering the dielectric structure being different for the various angles of incidence, entrained dispersion and intrinsic diffraction of the initial pulse to manifest differently. The computations were run until the sampled field amplitudes were extinguished to less than 2.5% of the amplitude of the initial pulse. Figure 5.2 shows intensity plots of the electric field at different times during the computation (snapshots) and the sampled data.

The post-processing steps of NFFFT and *Fourier*-transformation to the frequency domain of the sampled data were performed for each sampling window separately and to the same numerical accuracy of the FDTD calculations. All measured points were included in these computations and the NFFFT was executed for directions of propagation at intervals of 1° over the whole scattering hemicycle of a window. Once *Fourier*-transformed the data exhibited a spectral resolution smaller than $3nm$ in the visible range of wavelengths.

For each quadrant of the reciprocal space, *i.e.* the cycle of the directions of propagation with respect to the direction of the incident pulse, the contributions of the two windows neighbouring a vertex of the sampling rectangle were added using equation 2.6. All values were then normalised to the total power sampled in all directions of propagation at each wavelength. Finally, the back-scattered field was represented in a two-dimensional spectrogram, on the axes of which are the direction of propagation with respect to the normal to the structure surface, and the wavelength.

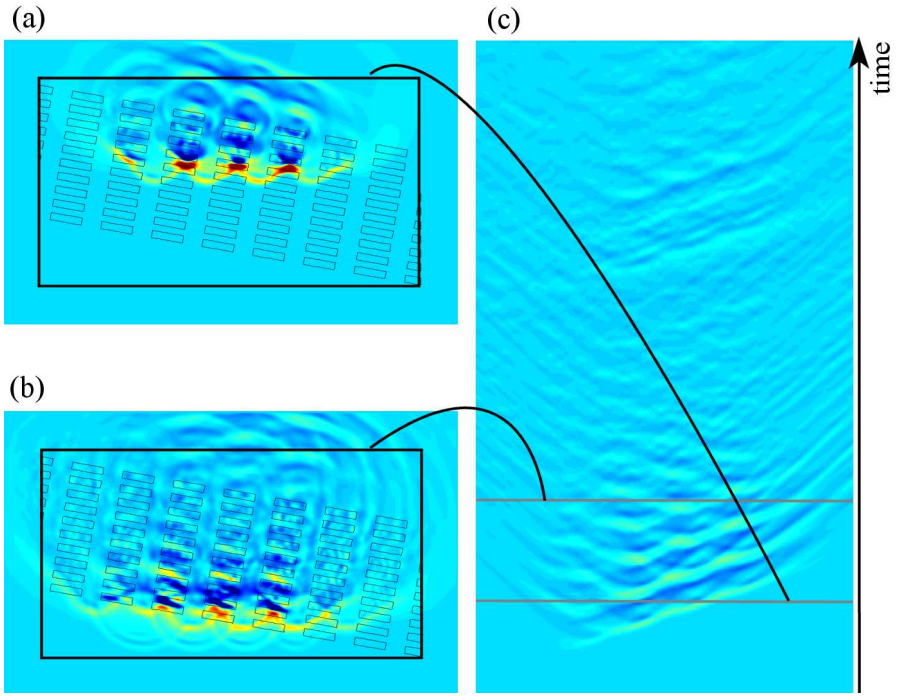

Figure 5.2: Example of a typical simulation: intensity plots of computed electric field after 250 (a) and 500 time steps (b) from the beginning of the computation (snapshots), and intensity plot of the field sampled at the top sampling window throughout the simulation (c). The gray lines correspond to the field sampled at the times of (a) and (b).

The same FDTD core algorithm employed in the present study has been previously used in the theoretical analysis of two-dimensional photonic crystal and photonic quasicrystal microstructures and successfully predicted the optical properties of fabricated devices. Those investigations were reported by Charlton *et al.* [100, 101] and Zoorob *et al.* [102, 103].

The computational tool composed of both the FDTD and NFFFT algorithms was tested comparing results of computations performed on a stack of layers with the transfer matrix method (TMM). This technique has been discussed in section 1.4 and is presented in appendix C. It was used here to compute the reflection of a stack of 10 layers of chitin (index of refraction 1.56) with a period of $180nm$ for an angle of incidence of $10°$, and a comparison between results obtained with the FDTD/NFFFT algorithms and the

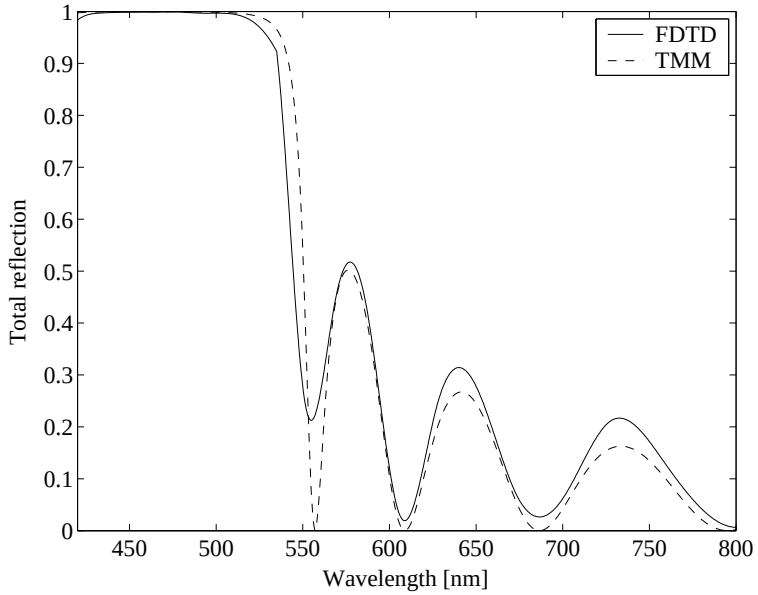

Figure 5.3: Comparison of the FDTD/NFFFT algorithm with TMM. Total reflection of a stack of chitin ($n = 1.56$) layers computed by FDTD/NFFFT and TMM.

TMM is shown in the plot of figure 5.3.

The numerical method to compute the efficiencies of diffraction orders in the reflection regime was put to the test by comparing the results with data published by Sakoda [57]. The two-dimensional expansion method used by Sakoda was proven accurate in the prediction of the reflection properties of triangular lattices of holes in dielectric, for frequencies in the bandgap region by Labilloy *et.al.* [58] in an experimental investigation. For frequencies above the bandgap, the computations predicted higher values of reflection than experimentally found. The FDTD/NFFFT method was applied for a structure presented in Sakoda's paper: a triangular lattice of air circles in a slab of dielectric constant of 2.1. The light impinged normally on a 7 unit cells thick crystal strip having the $\Gamma - \mathrm{J}$ reciprocal lattice axis perpendicular to its surface. The results reported by Sakoda (in figure 4 of his paper) and those obtained with our numerical method are shown in figure 5.4, respectively in the top and bottom plot. The curves with full markers correspond to the

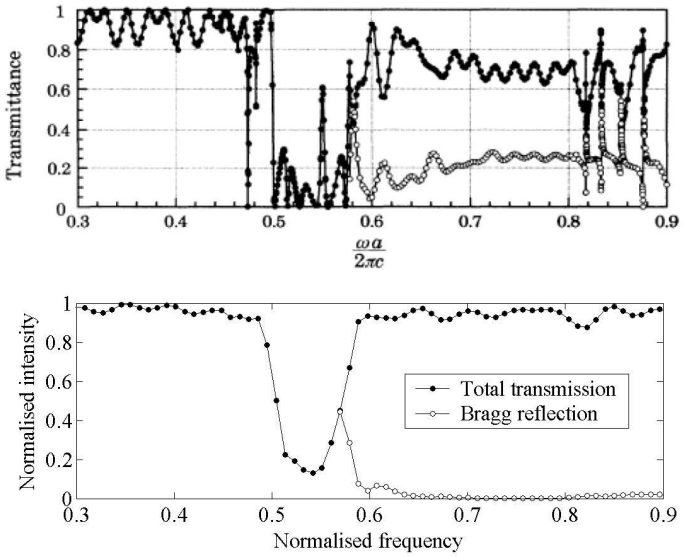

Figure 5.4: Comparison between transmissions and *Bragg* diffraction efficiencies obtained with expansion methods by Sakoda [57] (top plot) and with the numerical FDTD/NFFFT method (bottom plot).

total transmission of the structure, while the curves with empty markers correspond to the *Bragg* reflection, *i.e.* the sum of the diffraction orders higher than zero. Excellent agreement between the two methods is found for frequencies in the bandgap and below. At higher frequencies, Sakoda's results predict stronger diffraction and consequently lower transmission, as it did for the structures experimentally investigated by Labilloy *et.al.* The impinging pulse in the numerical computation was finite, as described above, and therefore interacted with a finite number of diffractive elements (approximately 15 unit cells). The effects of this finiteness were tested by comparison with a similar computation, performed using periodic boundary conditions and therefore an infinite number of elements. No substantial effect was observed on the efficiency of the diffracted orders in the reflection regime.

The accurate computation of reflections and diffraction efficiencies by numerical methods has been demonstrated. The effects of the finiteness of the initial pulse for the generation of diffraction efficiencies in the reflection regime when compared with an infinitely extended initial condition are neg-

ligible. The discrepancies between results obtained with expansion methods and the numerical method will be irrelevant for the present study, since only efficiencies at frequencies in the bandgap and below will be considered.

5.2 The diffraction of *Morpho*-type dielectric structures

The optical properties of the wings of *Morpho rhetenor* were studied using the computational technique presented in section 5.1. This study was consequently limited to two-dimensional models of the microstructure found on the wings of the butterfly, a restriction justified by the morphology of the natural structure but for the slanting of the branched ridges, which breaks the continuous translational symmetry (cf. section 1.2.2).

From TEM cross-sectional views of the butterfly microstructure (figure 1.2) one can see that it consists of a grating-like periodic arrangement, where each of the diffractive elements has the shape of a pine tree with evenly spaced branches of constant thickness, which results in a periodic layering. The width of the trees is quite constant at the bottom, with a linear filling fraction in the plane of the wing of approximately 0.8, but narrows towards the top. The arrangement of the branches around the stalk is essentially asymmetric (with a zigzag pattern), but the irregular bending of the stalks causes, in certain regions, opposed branches to be at the same height or facing each other if belonging to two different trees. The shape of the branches is with good approximation that of a rectangular slab. However, irregularities in the arrangement cause all dimensions to vary throughout the structure and make determining an absolutely valid model a subjective and inconclusive exercise. For this reason, the present study focussed on the evaluation of the importance, from the point of view of the optical phenomenology, of two fundamental morphological features of the microstructure occurring consistently over wide areas of the cross-section: the lattice and the tapering of the diffractive elements.

The fact that over large regions of the microstructure the branches either consistently face each other or are shifted by half a vertical period, permits one to identify two *Bravais* lattices inherent to these symmetries: a rectangular and a centered rectangular one.

Four different structures were studied numerically to identify which of the features pertaining to the distribution of dielectric in the microstructure on the wings of *Morpho rhetenor* is relevant to its phenomenology. All structures were composed of one dielectric having an index of refraction of 1.56 embedded in vacuum (or air). In this way, absorption was neglected, which however only affects the magnitude of waves and not their optical pathlengths, and therefore does not influence the interference mechanisms. The structures were: (a) a rectangular lattice of rectangular dielectric elements; (b) a tapered version of the above, resulting in a pine tree structure with its tips towards the incident front; (c) a centred rectangular lattice of rectangular dielectric elements; and (d) a tapered version of (c), resulting in an asymmetric pine tree structure. While cases (a) and (b) share the same lattice and so do (c) and (d), cases (a) and (c) share the same area filling fraction and so do (b) and (d). Figure 5.5 shows four schematic views of the above mentioned arrangements of dielectric.

A preliminary investigation of the effects on the reflectivity of a structure of type (b) caused by changing the linear filling fractions and the periods for normally incident light, revealed that no qualitative unexpected effects arise from such variations. Changing the lateral periods causes the power to be distributed differently amongst the orders of diffraction, but the position of the long-wavelength edge of a high-reflectivity band does not vary. The normalised reflectances of structures of type (b) with a normal period of $180nm$ and lateral periods varying between $525nm$ and $825nm$ are shown in the plot on the left-hand side of figure 5.6. Changing the vertical period shifts the centre of the high-reflectivity band by a factor determined by the period itself, similarly to a multilayer arrangement. The normalised reflectances of structures of type (b) with a lateral period of $675nm$ and normal periods of

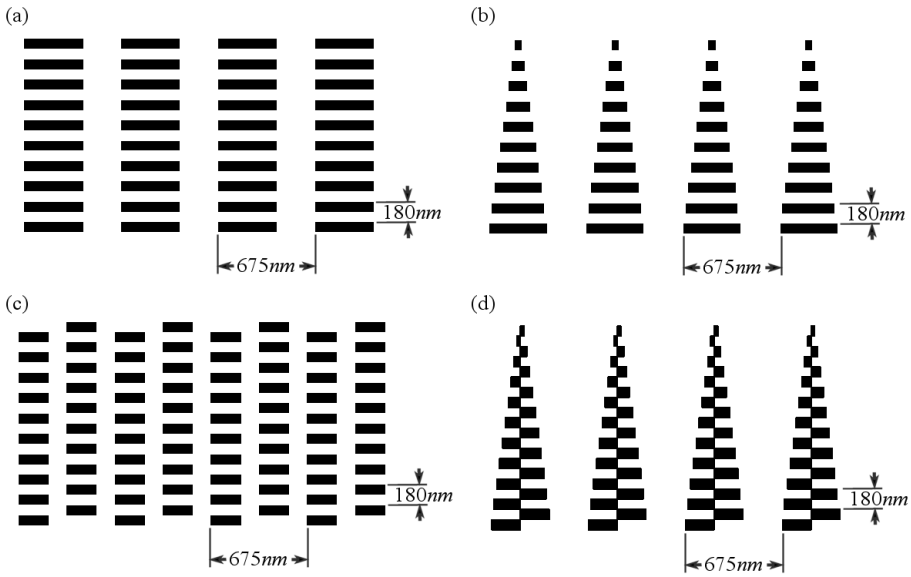

Figure 5.5: Schematic views of the dielectric structures studied numerically: (a) a rectangular lattice of rectangular dielectric elements; (b) a tapered version of the above, resulting in a pine tree structure with its tips towards the incident front; (c) a centred rectangular lattice of rectangular dielectric elements; and (d) a tapered version of (c), resulting in an asymmetric pine tree structure.

140, 160, 180, 200 and 220nm are shown in the plot on the right-hand side of figure 5.6; on the horizontal axis the wavelength has been scaled to the ratio 180nm/period to highlight the strict relation between the position of the mentioned band edge and the normal period.

Hence, average values were used for the geometrical parameters (periods and filling fractions) of the four structures introduced above. The periods along the orthogonal axes of the lattices were 675nm along the width of the structures (large period) and 180nm along their height (small period), with a total of 10 periods/elements in the latter direction. All dielectric elements in the structures were oriented along the orthogonal axes of the lattices.

For each structure, computations of the diffracted field have been performed for three angles of incidence (10°, 30° and 60°) and both polarisations (TE and TM). For all cases, filled contour plots of the angle-dependent spectrograms and plots of the diffraction efficiencies are shown below.

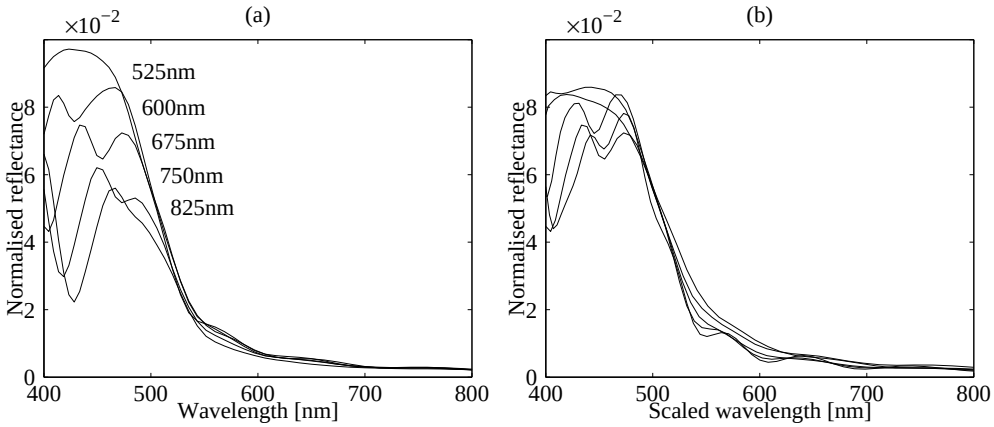

Figure 5.6: Specular reflection of rectangular structures with different periods at normal incidence and TE polarisation. Plot (a) shows the effects of varying the lateral period and (b) show the reflectance of structures with different normal periods, whereby the wavelengths are scaled to the normal period.

5.2.1 Rectangular lattice

The diffracted field was computed for a rectangular lattice of rectangular elements (plot (a) in figure 5.5), having a large period and corresponding linear filling fraction of $675nm$ and 0.6, respectively, and a small period and corresponding linear filling fraction of $180nm$ and 0.5, respectively. The resulting area filling fraction was 0.3. Filled contour plots of the angle-dependent spectrograms and plots of the diffraction efficiencies are shown in figures 5.8 and 5.9. All reported values are normalised to the sum of the sampled field intensity for all directions of propagation at each wavelength.

A plot of the total reflections for all angles of incidence and for the TE polarisation is shown on the left-hand side of figure 5.7, while the corresponding plot for the TM polarisation is found on the right-hand side of the same figure. A plateau is found in the short-wavelength range of the visible spectrum (at wavelengths shorter than $540nm$ and $510nm$ for the TE and TM polarisation, respectively) for the smaller angles of incidence, with total reflections larger than 75% for both polarisations and 10° incidence. The structure in this respect acts as a high-pass filter, similarly to a dielectric mirror and shows a high reflection despite its low filling fraction. At larger

angles of incidence the high-reflection band disappears and very modulated spectra are found. For the TE polarisation, the maximum total reflection decreases to 70% and 60% for 30° and 60°, respectively, while for the TM polarisation it is more severely reduced. This strong change in total reflection is related to the dramatic variation of the 0^{th} order of diffraction (or specular reflection), where the 1^{st} order of diffraction maintains similar intensities and for the smaller angles of incidence similar spectral contents. So, while much of the back-scattered power is found in the 0^{th} order for the TE polarisation and all angles of incidence, a transfer of power increasingly into the 1^{st} order occurs for the TM polarisation with increasing angle of incidence. The diffracted light is strongly polarised for the largest angle of incidence, similarly to the dielectric mirror, but unlike the stack, also for 30° incidence.

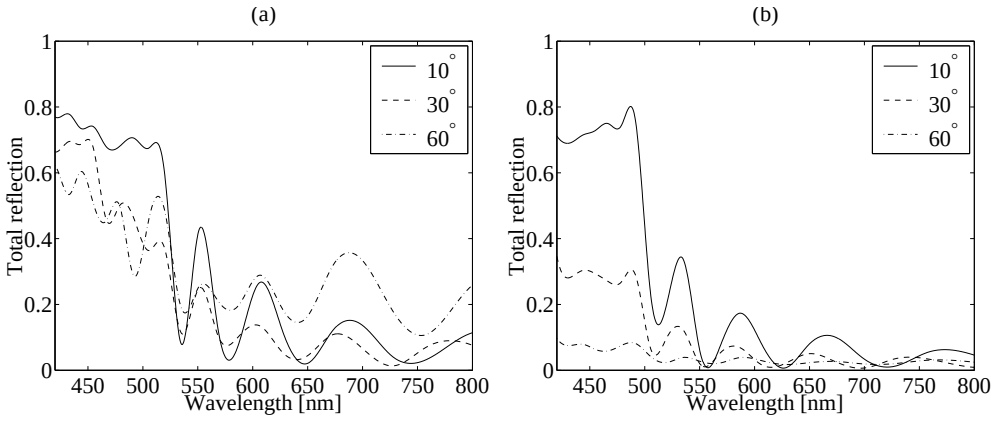

Figure 5.7: Total reflection of rectangular structures at different angles of incidence and polarisation. Plot (a) shows the results for TE polarisation and (b) for TM polarisation.

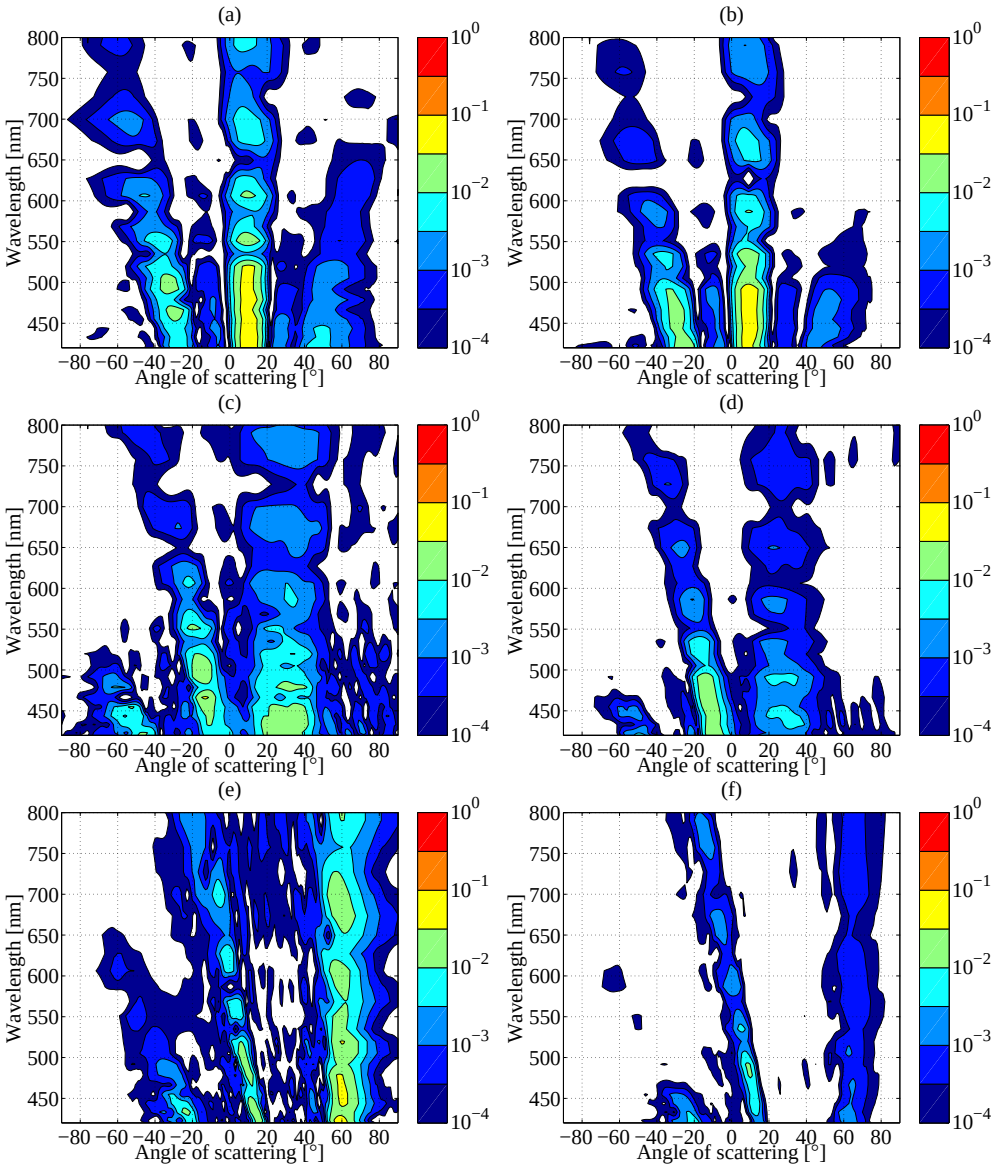

Figure 5.8: Filled contour plots of the computed back-scattering of a straight, rectangular *Morpho*-type structure at different angles of incidence and polarisation. Plots (a) and (b) show the results for 10° incidence, (c) and (d) for 30° incidence, (e) and (f) for 60° incidence. In plots (a), (c) and (e) the incident pulse is TE polarised, in (b), (d) and (f) TM polarised. All values are normalised to the total sampled power.

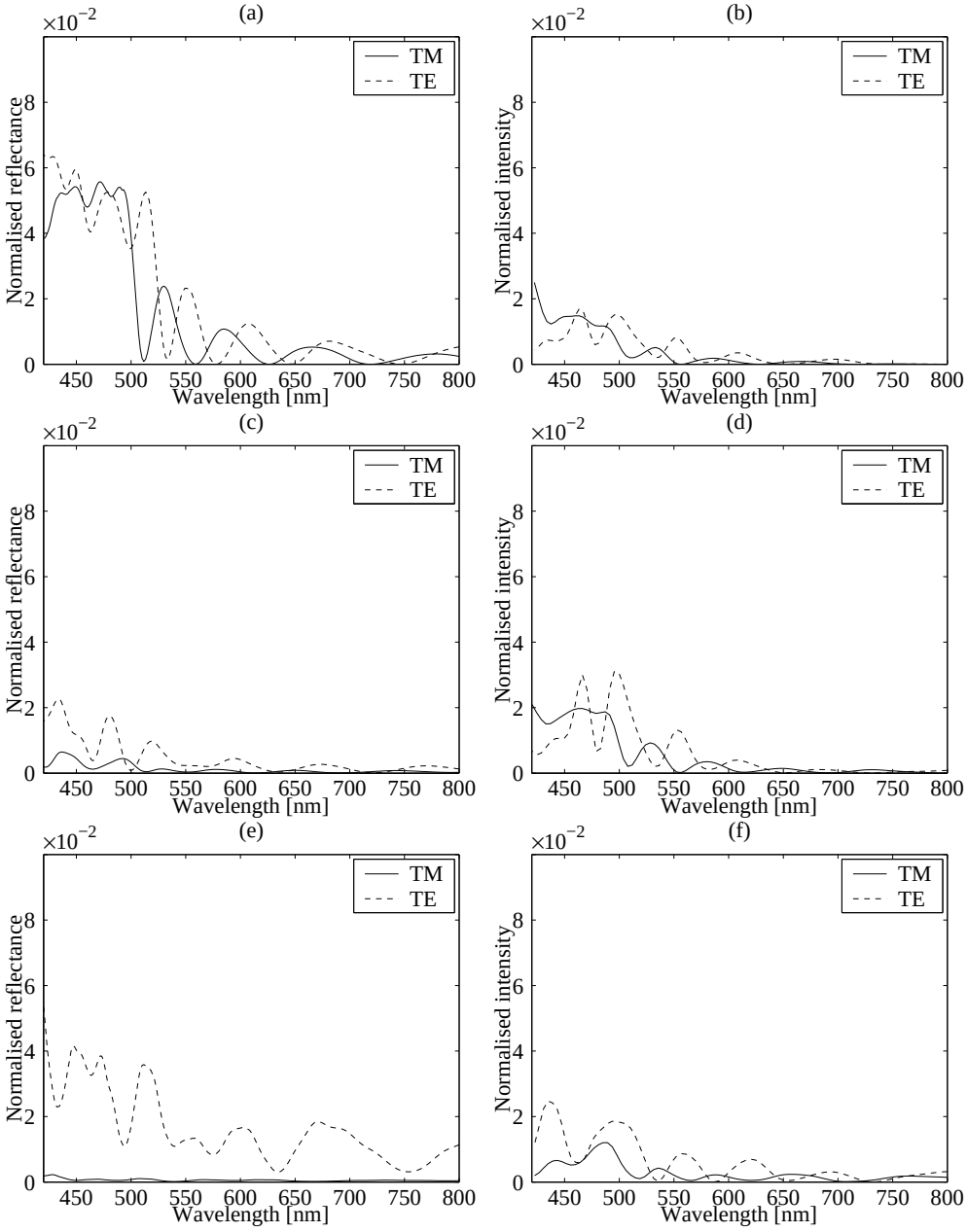

Figure 5.9: Computed spectra of the diffraction orders of a straight, rectangular *Morpho*-type structure at different angles of incidence and polarisation. Plots (a), (c) and (e) show the 0^{th} diffraction order, or specular reflection, for an angle of incidence of 10°, 30° and 60°, respectively. Plots (b), (d) and (f) show the corresponding 1^{st} diffraction orders. All values are normalised to the total sampled power.

5.2.2 Tapered rectangular structures

The diffracted field was computed for a rectangular lattice of rectangular elements with tapered width of the diffractive elements (plot (b) in figure 5.5). The large period was $675nm$, and the small period and its corresponding linear filling fraction were $180nm$ and 0.5, respectively. The filling fraction along the height of the diffractive elements was linearly decreased from 0.6 to 0.07 from bottom to top of the tree structures. Filled contour plots of the angle-dependent spectrograms and plots of the diffraction efficiencies are shown in figures 5.10 and 5.11. All reported values are normalised to the sum of the sampled field intensity for all directions of propagation at each wavelength.

A plot of the total reflections for all angles of incidence and for the TE polarisation is shown on the left-hand side of figure 5.12, while the corresponding plot for the TM polarisation is found on the right-hand side of the same figure. Most of the back-scattered light is found in the short-wavelength range of the visible spectrum (at wavelengths shorter than $540nm$ and $510nm$ for the TE and TM polarisation, respectively) for the smaller angles of incidence, with very high total reflection maxima, 89% and 72% for TE and TM polarisations, at the lowest angle of incidence. The reflected power however dramatically decreases for larger angles of incidence. The decrease in total reflection is due to a rapid change in specular reflection with increasing angle of incidence, which irrespective of the polarisation is almost extinct for both the larger angles. Most of the back-scattered power is concentrated in the 1^{st} order of diffraction for the middle angle of incidence. For equal polarisations, the spectral content of this order is very similar for angles of incidence of $10°$ and $60°$. In comparison to the structure discussed in section 5.2.1, both arrangements have qualitatively similar spectra, but for the tapered structure they appear less modulated, with wide and smooth peaks, resulting from a more gentle slope at the side of the high-reflection ranges of wavelengths and form a flatter local modulation.

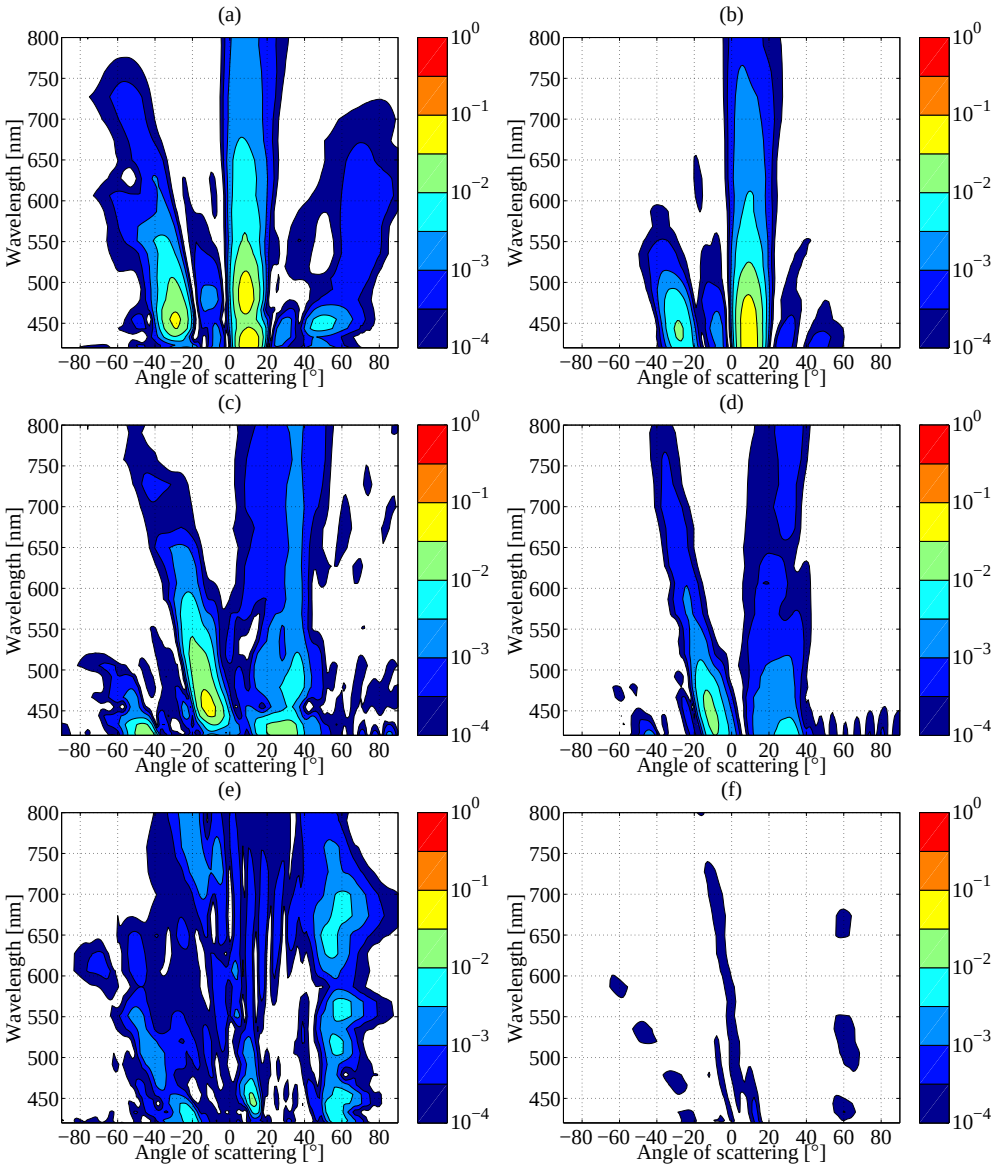

Figure 5.10: Filled contour plots of the computed back-scattering of a tapered, rectangular *Morpho*-type structure at different angles of incidence and polarisation. Plots (a) and (b) show the results for 10° incidence, (c) and (d) for 30° incidence, (e) and (f) for 60° incidence. In plots (a), (c) and (e) the incident pulse is TE polarised, in (b), (d) and (f) TM polarised. All values are normalised to the total sampled power.

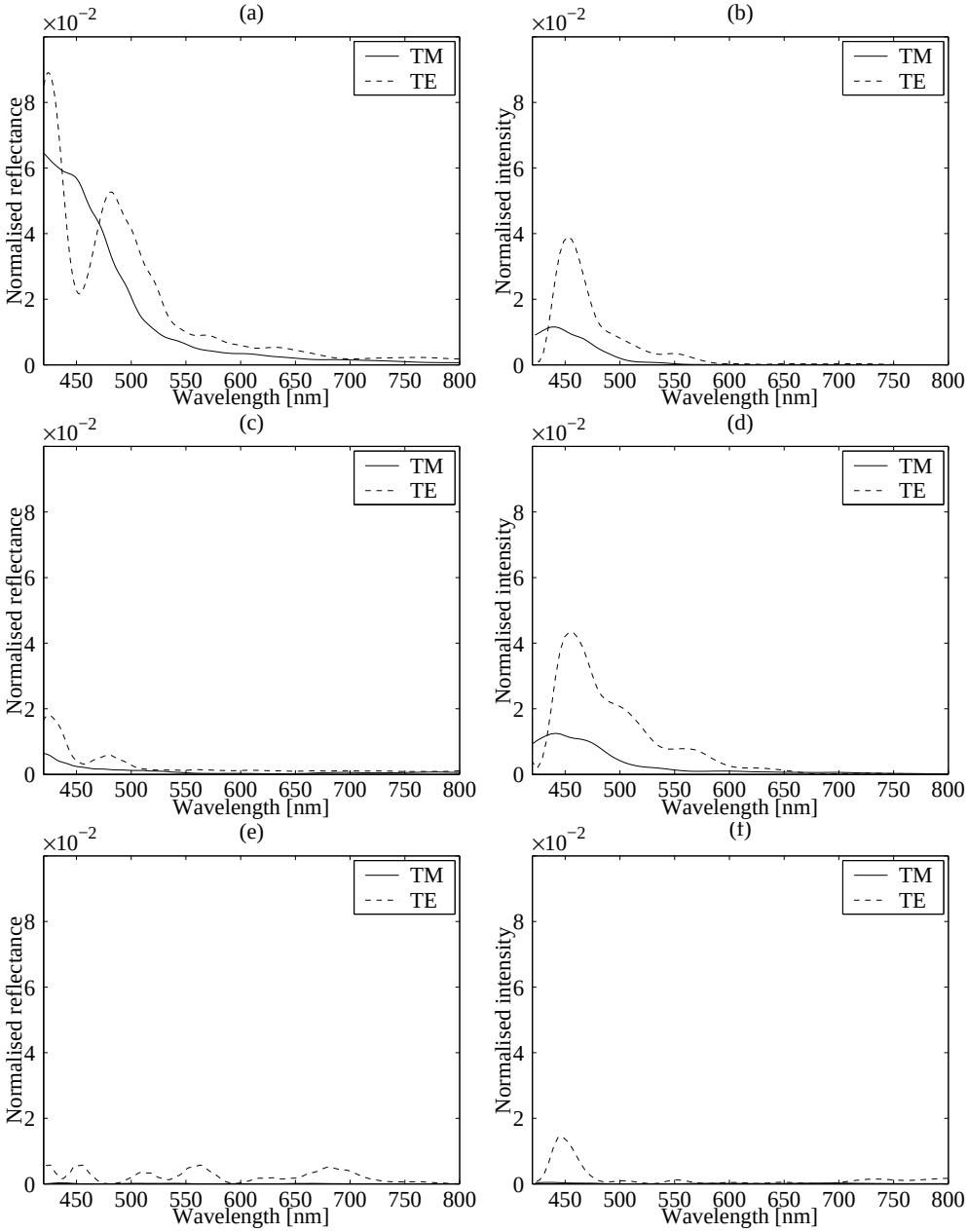

Figure 5.11: Computed spectra of the diffraction orders of a tapered, rectangular *Morpho*-type structure at different angles of incidence and polarisation. Plots (a), (c) and (e) show the 0^{th} diffraction order, or specular reflection, for an angle of incidence of 10°, 30° and 60°, respectively. Plots (b), (d) and (f) show the corresponding 1^{st} diffraction orders. All values are normalised to the total sampled power.

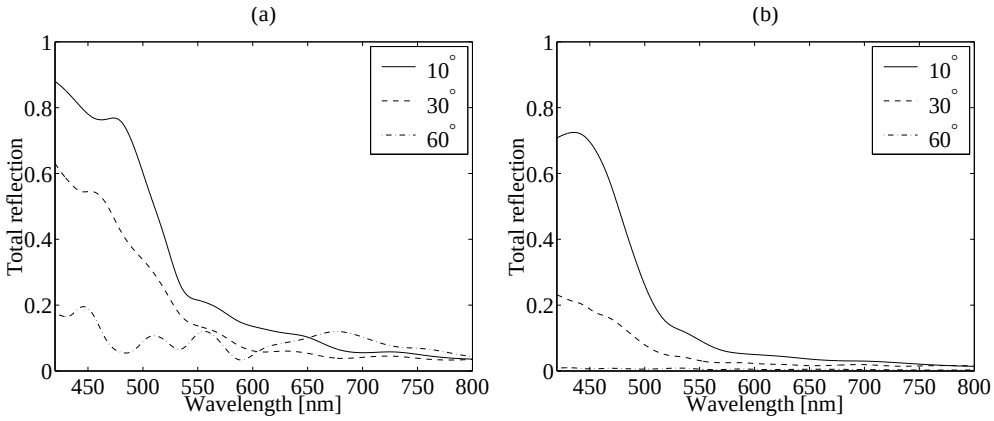

Figure 5.12: Total reflection of tapered rectangular structures at different angles of incidence and polarisation. Plot (a) shows the results for TE polarisation and (b) for TM polarisation.

5.2.3 Centred rectangular lattice

The diffracted field was computed for a centred rectangular lattice of rectangular elements (plot (c) in figure 5.5), having a large period of $675nm$ and a small period of $180nm$. The linear filling fraction along the normal to the structure surface was 0.5 and the area filling fraction was 0.3, the same values as the structures with a rectangular lattice discussed in section 5.2.1. Filled contour plots of the angle-dependent spectrograms and plots of the diffraction efficiencies are shown in figures 5.14 and 5.15. All reported values are normalised to the sum of the sampled field intensity for all directions of propagation at each wavelength.

A plot of the total reflections for all angles of incidence and for the TE polarisation is shown on the left-hand side of figure 5.13, while the corresponding plot for the TM polarisation is found on the right-hand side of the same figure. A plateau is found in the short-wavelength range of the visible spectrum (at wavelengths shorter than $490nm$ and $460nm$ for the TE and TM polarisation, respectively) for the smaller angles of incidence, with total reflections larger than 90% for both polarisations and 10° incidence. For the TE polarisation, the maximum total reflection decreases to 73% and 51%

for 30° and 60°, respectively, while for the TM polarisation and the same angles of incidence it decreases to 80% and 13%. For all cases of incidence and polarisation most of the back-scattered power is found in the 1st order of diffraction with comparatively very small values of the field in the direction of specular reflection, with the exception of 60° and TE polarisation. For all angles of incidence the diffracted light is strongly polarised.

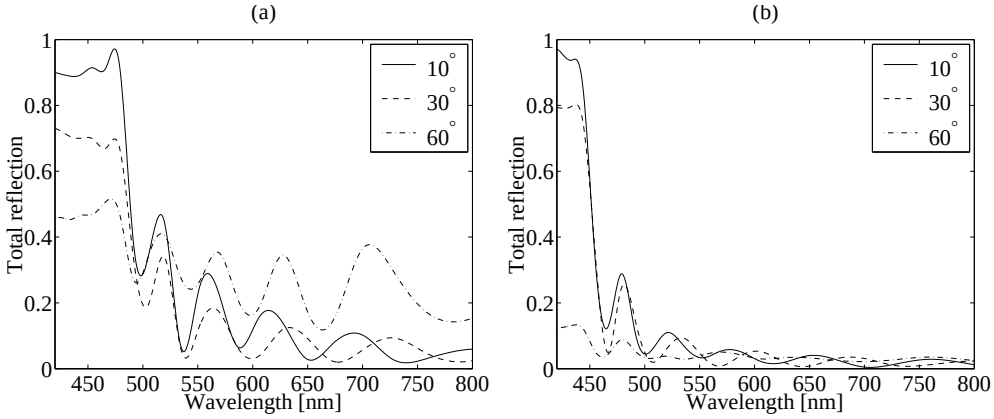

Figure 5.13: Total reflection of centred rectangular structures at different angles of incidence and polarisation. Plot (a) shows the results for TE polarisation and (b) for TM polarisation.

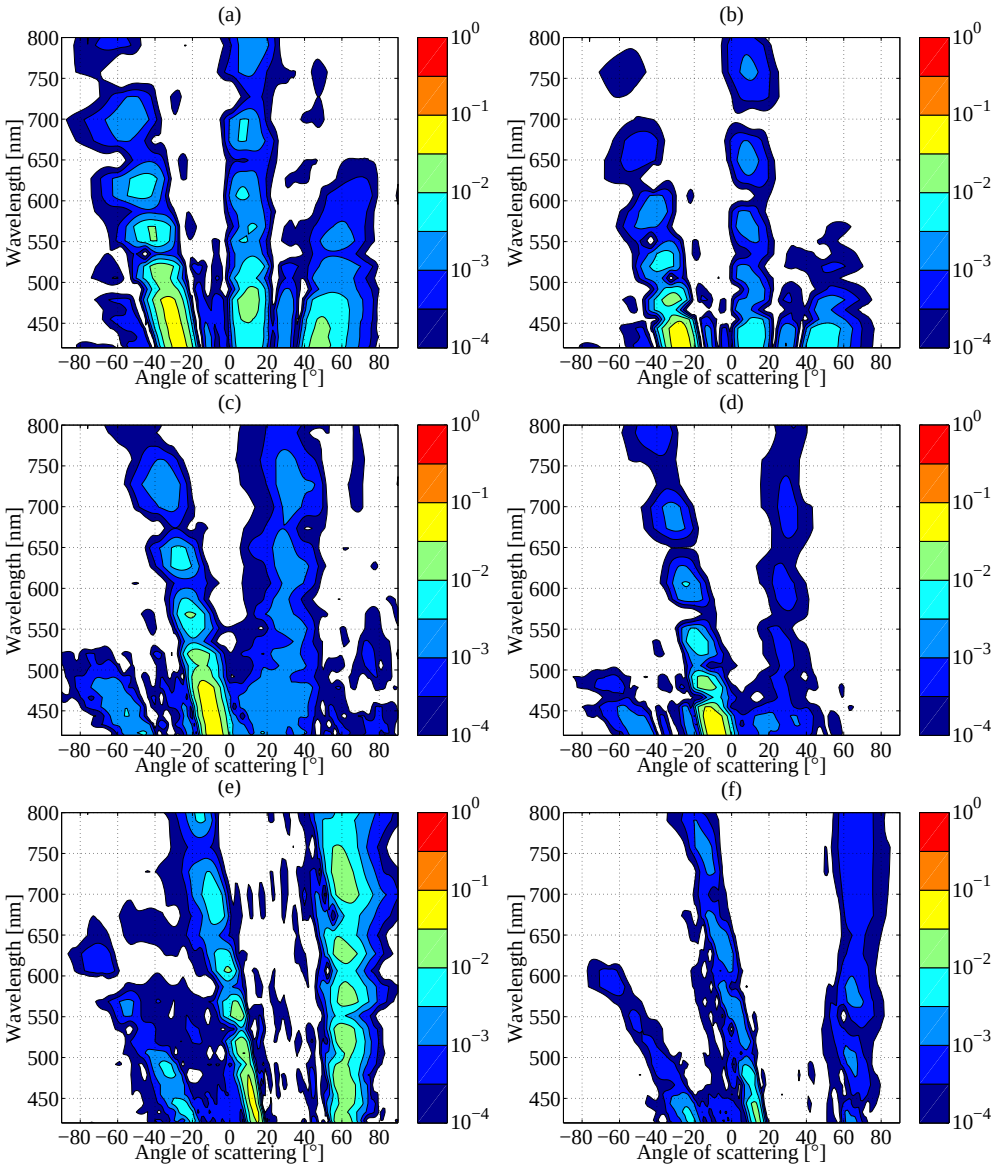

Figure 5.14: Filled contour plots of the computed back-scattering of a straight, centred rectangular *Morpho*-type structure at different angles of incidence and polarisation. Plots (a) and (b) show the results for 10° incidence, (c) and (d) for 30° incidence, (e) and (f) for 60° incidence. In plots (a), (c) and (e) the incident pulse is TE polarised, in (b), (d) and (f) TM polarised. All values are normalised to the total sampled power.

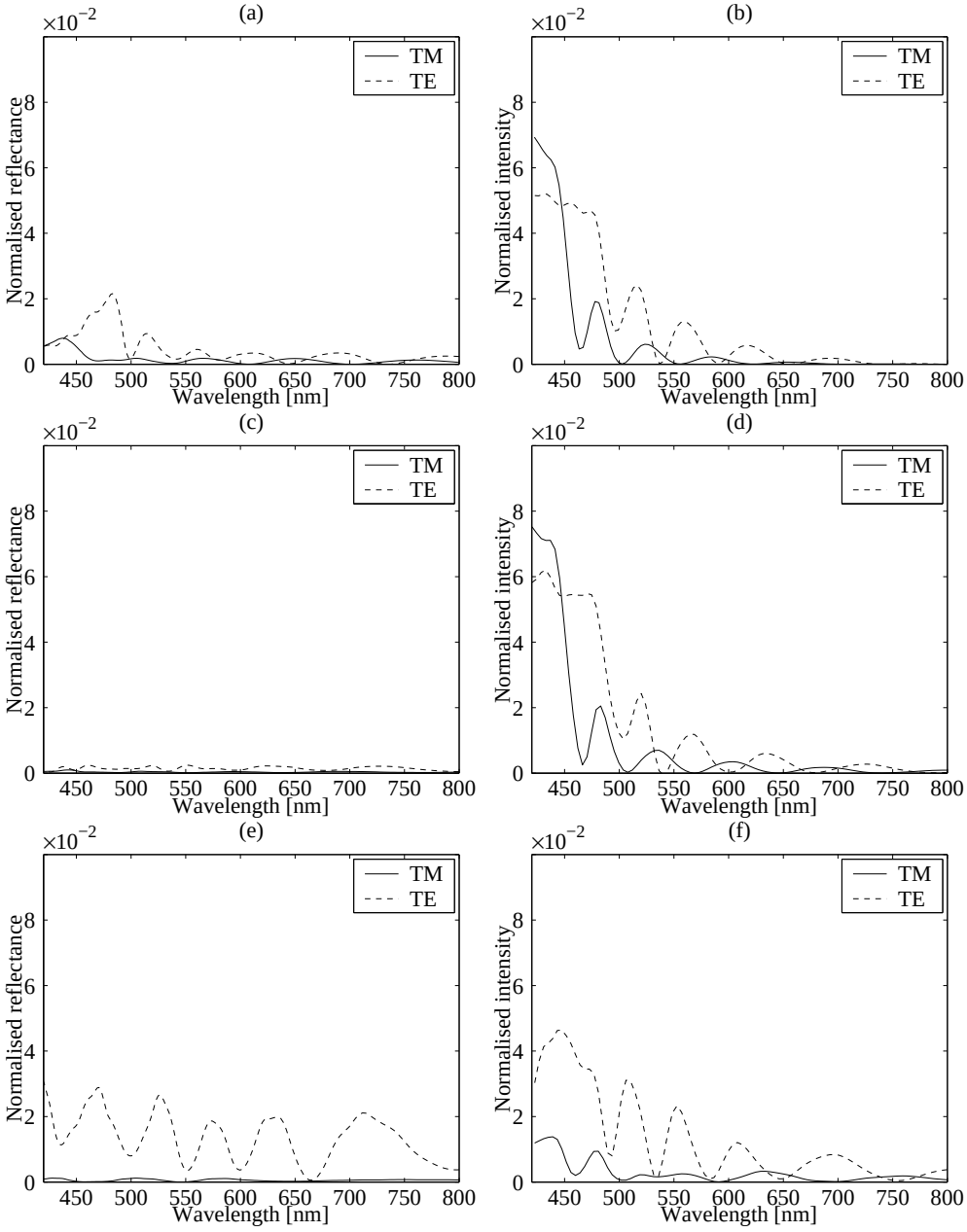

Figure 5.15: Computed spectra of the diffraction orders of a straight, centred rectangular *Morpho*-type structure at different angles of incidence and polarisation. Plots (a), (c) and (e) show the 0^{th} diffraction order, or specular reflection, for an angle of incidence of 10°, 30° and 60°, respectively. Plots (b), (d) and (f) show the corresponding 1^{st} diffraction orders. All values are normalised to the total sampled power.

5.2.4 Asymmetric tapered structure

The diffracted field was computed for a centred rectangular lattice of rectangular elements with tapered widths of the diffractive elements (plot (d) in figure 5.5). The large period was $675nm$ and the small period $180nm$. The tapering of the pine tree structure and the filling fractions were the same of the tapered structures with a rectangular lattice discussed in section 5.2.2. Filled contour plots of the angle-dependent spectrograms and plots of the diffraction efficiencies are shown in figures 5.16 and 5.17. All reported values are normalised to the sum of the sampled field intensity for all directions of propagation at each wavelength.

A plot of the total reflections for all angles of incidence and for the TE polarisation is shown on the left-hand side of figure 5.18, while the corresponding plot for the TM polarisation is found on the right-hand side of the same figure. Most of the back-scattered light is found in the short-wavelength range of the visible spectrum (at wavelengths shorter than $490nm$ and $460nm$ for the TE and TM polarisation, respectively) for the smaller angles of incidence, with total reflection maxima of 87% and 58% for TE and TM polarisations, and for the smallest angle of incidence. For the TE polarisation, the maximum total reflection decreases to 64% and 21% for 30° and 60°, respectively, while for the TM polarisation and the same angles of incidence it decreases to 55% and 3%. The back-scattered power is almost entirely concentrated in the 1^{st} order of diffraction for all angles of incidence since the intensity of the specularly reflected light is several orders of magnitude smaller. For equal polarisations, the spectral content of this order is similar for angles of incidence of 10° and 30°. In comparison to the structure discussed in section 5.2.3, although the spectra are qualitatively similar for both arrangements, those for the tapered structure appear less modulated with wide and smooth peaks, resulting from a more gentle slope at the side of the high-reflection ranges of wavelengths and from a flatter local modulation.

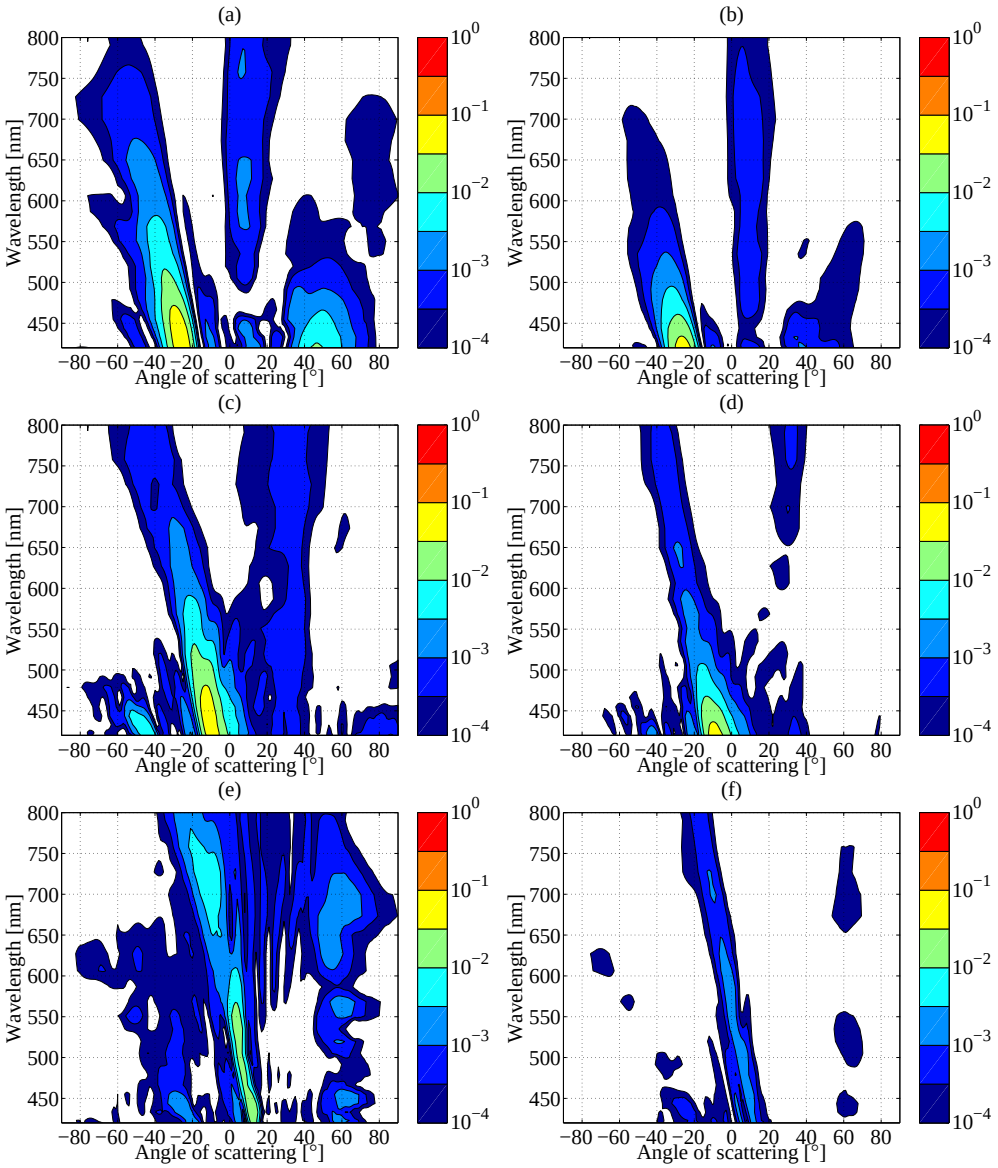

Figure 5.16: Filled contour plots of the computed back-scattering of a tapered, asymmetric *Morpho*-type structure at different angles of incidence and polarisation. Plots (a) and (b) show the results for 10° incidence, (c) and (d) for 30° incidence, (e) and (f) for 60° incidence. In plots (a), (c) and (e) the incident pulse is TE polarised, in (b), (d) and (f) TM polarised. All values are normalised to the total sampled power.

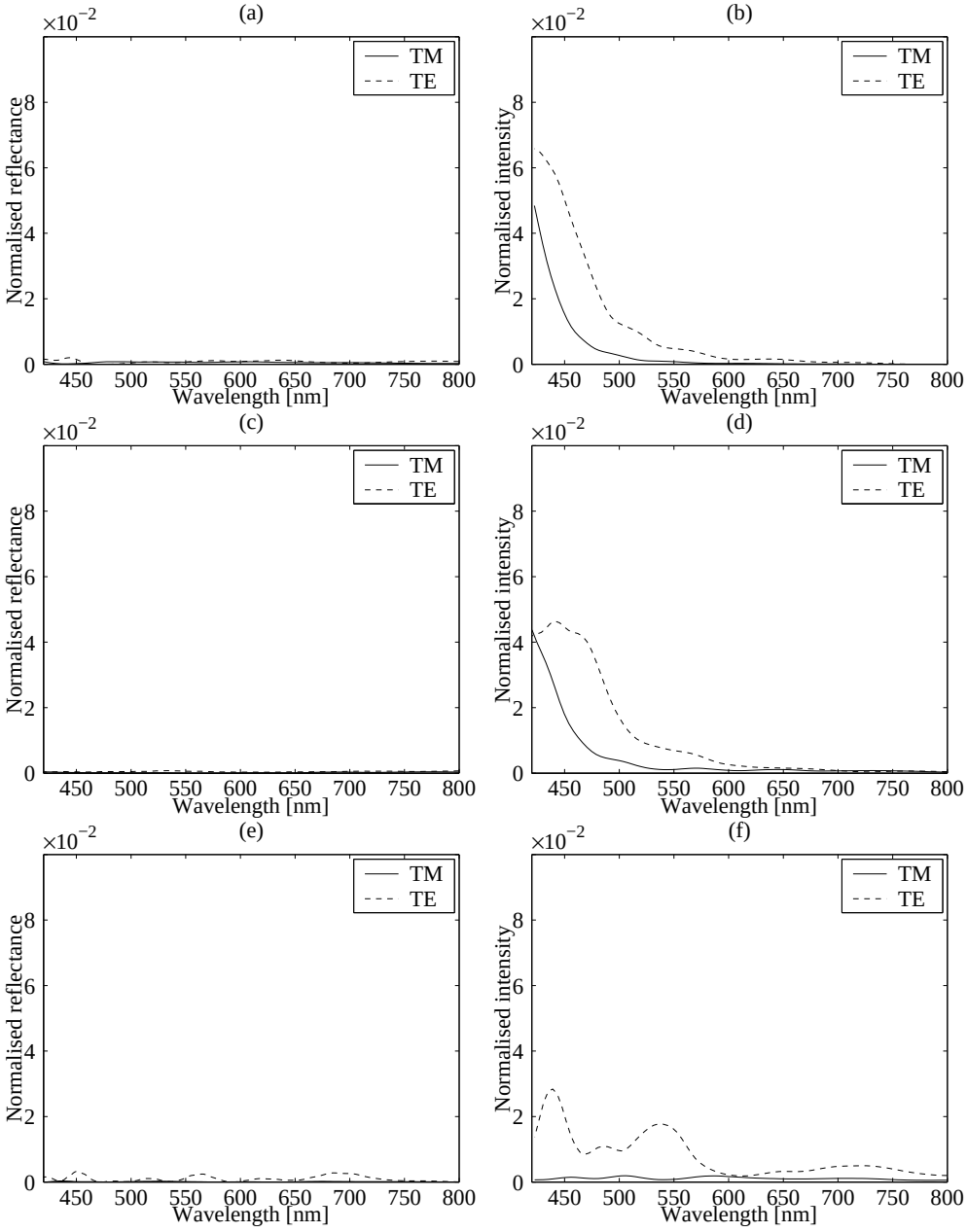

Figure 5.17: Computed spectra of the diffraction orders of a tapered, asymmetric *Morpho*-type structure at different angles of incidence and polarisation. Plots (a), (c) and (e) show the 0^{th} diffraction order, or specular reflection, for an angle of incidence of 10°, 30° and 60°, respectively. Plots (b), (d) and (f) show the corresponding 1^{st} diffraction orders. All values are normalised to the total sampled power.

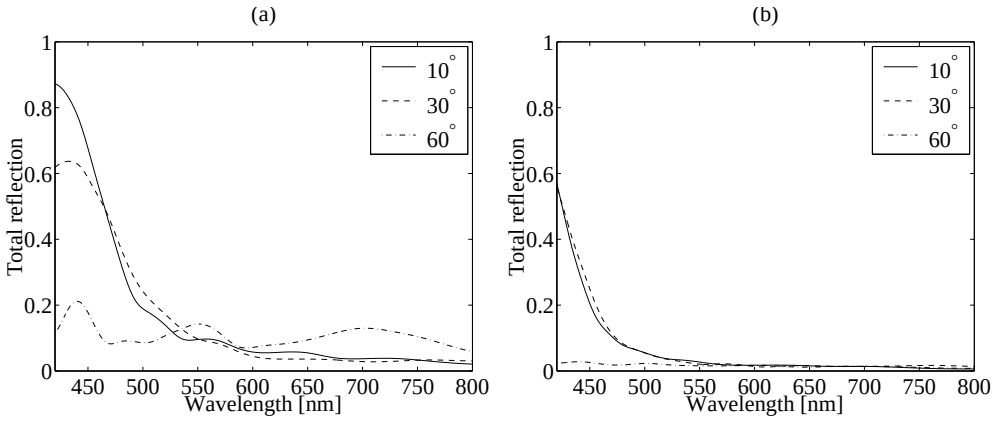

Figure 5.18: Total reflection of tapered asymmetric structures at different angles of incidence and polarisation. Plot (a) shows the results for TE polarisation and (b) for TM polarisation.

5.3 The diffraction of SiO_2/Si_3N_4 lamellar volume diffractive structures

The diffraction of lamellar volume diffractive structures composed of layered diffractive elements made of silicon dioxide (SiO_2, index of refraction 1.46) and silicon nitride (Si_3N_4, index of refraction 2.02) was also computed numerically. This investigation was aimed at modelling the fabricated structures presented in section 3.3 and to compare their properties with *Morpho*-type diffractive arrangements. However, the substrate and the buffer layer of the real structures was not included in the computation because of the excessive computational load involved, which meant that parts of the spectrum where low reflection occurs would not compare with experimental results on the fabricated devices, where the high index substrate also generates strong reflection. The studied structures were similar to those schematically shown in plots (a) and (b) of figure 5.5, but each diffractive element was a connected stack of 20 layers of SiO_2 and Si_3N_4. This corresponds to structures defined by etching either straight or funnel-shaped trenches in a dielectric mirror, thus resulting in grating-like devices with straight or tapered diffractive elements.

The large period was $510nm$, the thickness of the SiO_2 and Si_3N_4 layers was $74nm$ and $102nm$, respectively, resulting in a small period of $176nm$. The linear filling fraction along the width of the straight structure was 0.78, and varied between 0.78 and 0.1 for the tapered version. Filled contour plots of the angle-dependent spectrograms and plots of the diffraction efficiencies are shown in figures 5.19 to 5.22. All reported values are normalised to the sum of the sampled field intensity for all directions of propagation at each wavelength.

For straight lamellar gratings, the total reflection largely consists of specular reflection and has a spectral content similar to a dielectric mirror for an angle of incidence of 10° and both polarisations. While the maxima of the total reflection (shown in figure 5.23) remain high for larger angles of incidence and TE polarisation, more structured spectra are found in these cases for both polarisations and the spectra obtained differ strongly from dielectric mirrors. For the TE polarisation, maximum total reflections higher than 90% are found for all angles of incidence, while for TM polarised light they vary from more than 90% to less than 60% and 30% for a change in angle of incidence from 10° through 30° to 60°, thus generating a strongly polarised reflection. An interesting strong feature is present around $470nm$ for an angle of incidence of 60° and TM polarisation in the specular reflection which coexists with strong diffraction in the 1^{st} order at longer wavelengths.

For tapered lamellar gratings, much of the back-scattered power is found in the 1^{st} order of diffraction. Again the structures have similar spectra to the straight ones in total reflection (shown in figure 5.24), the main difference consisting in wider and smoother peaks with a marked long-wavelength suppression of any modulation. Here however, as opposed to the effects of tapering on *Morpho*-type structures discussed in section 5.2.2, the orders of diffraction behave in a substantially different manner from the straight structures. Strong and quite narrow peaks are found for the 1^{st} order of diffraction at wavelengths smaller than $600nm$, which do not occur in the straight structures, and efficiencies vary sensibly for different polarisations.

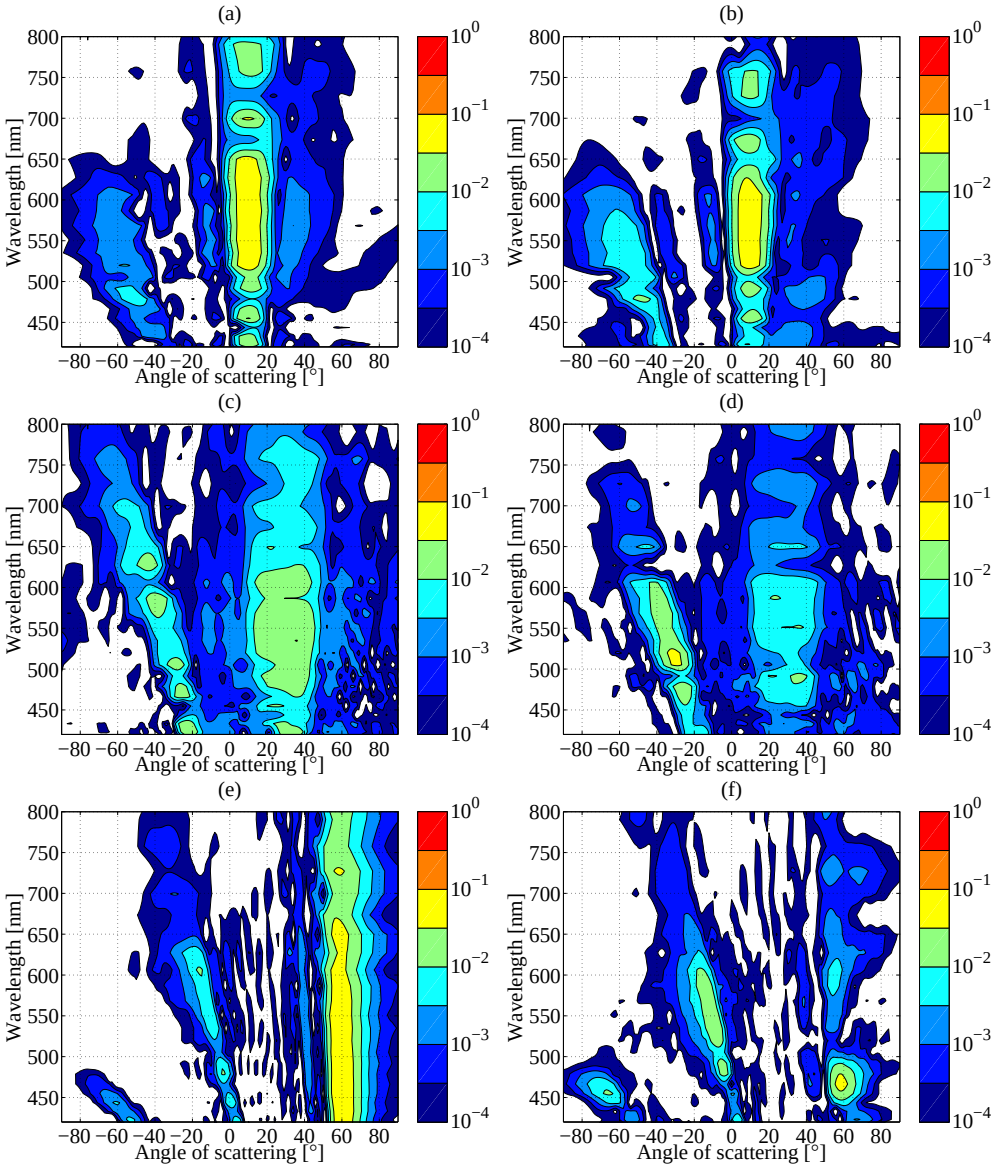

Figure 5.19: Filled contour plots of the computed back-scattering of a straight lamellar volume diffractive structure with layered diffractive elements at different angles of incidence and polarisation. Plots (a) and (b) show the results for 10° incidence, (c) and (d) for 30° incidence, (e) and (f) for 60° incidence. In plots (a), (c) and (e) the incident pulse is TE polarised, in (b), (d) and (f) TM polarised. All values are normalised to the total sampled power.

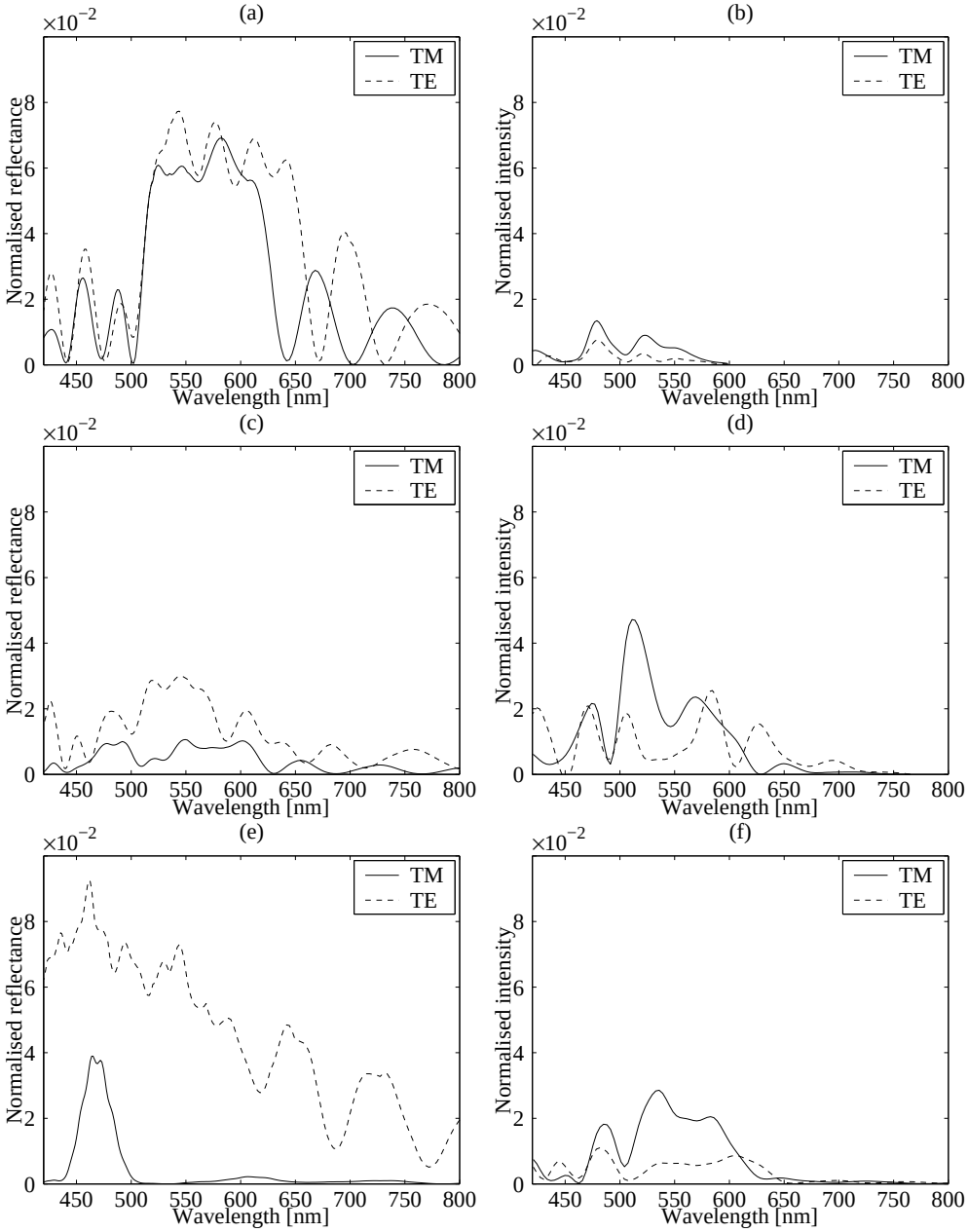

Figure 5.20: Computed spectra of the diffraction orders of a straight lamellar volume diffractive structure with layered diffractive elements at different angles of incidence and polarisation. Plots (a), (c) and (e) show the 0^{th} diffraction order, or specular reflection, for an angle of incidence of 10°, 30° and 60°, respectively. Plots (b), (d) and (f) show the corresponding 1^{st} diffraction orders. All values are normalised to the total sampled power.

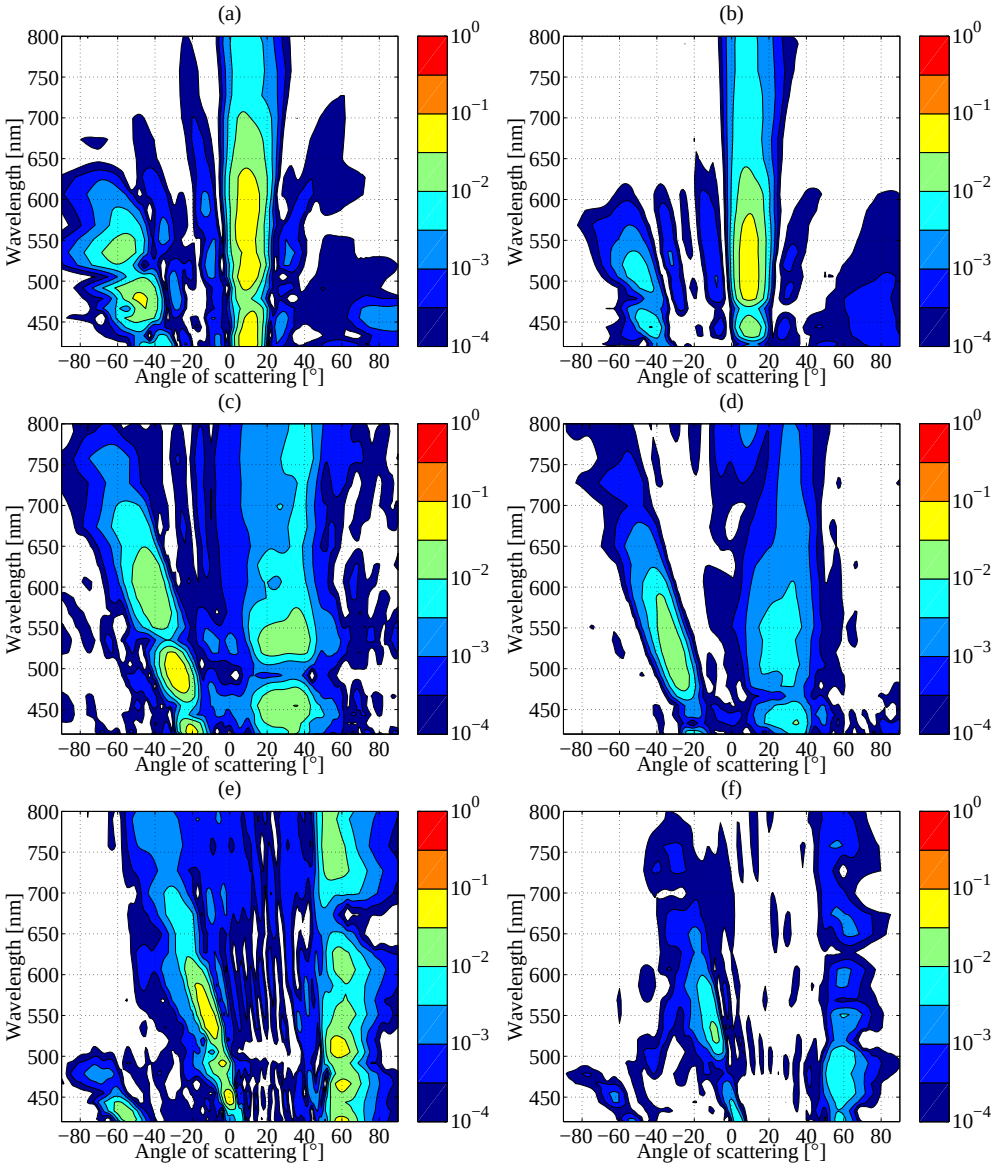

Figure 5.21: Filled contour plots of the computed back-scattering of a tapered lamellar volume diffractive structure with layered diffractive elements at different angles of incidence and polarisation. Plots (a) and (b) show the results for 10° incidence, (c) and (d) for 30° incidence, (e) and (f) for 60° incidence. In plots (a), (c) and (e) the incident pulse is TE polarised, in (b), (d) and (f) TM polarised. All values are normalised to the total sampled power.

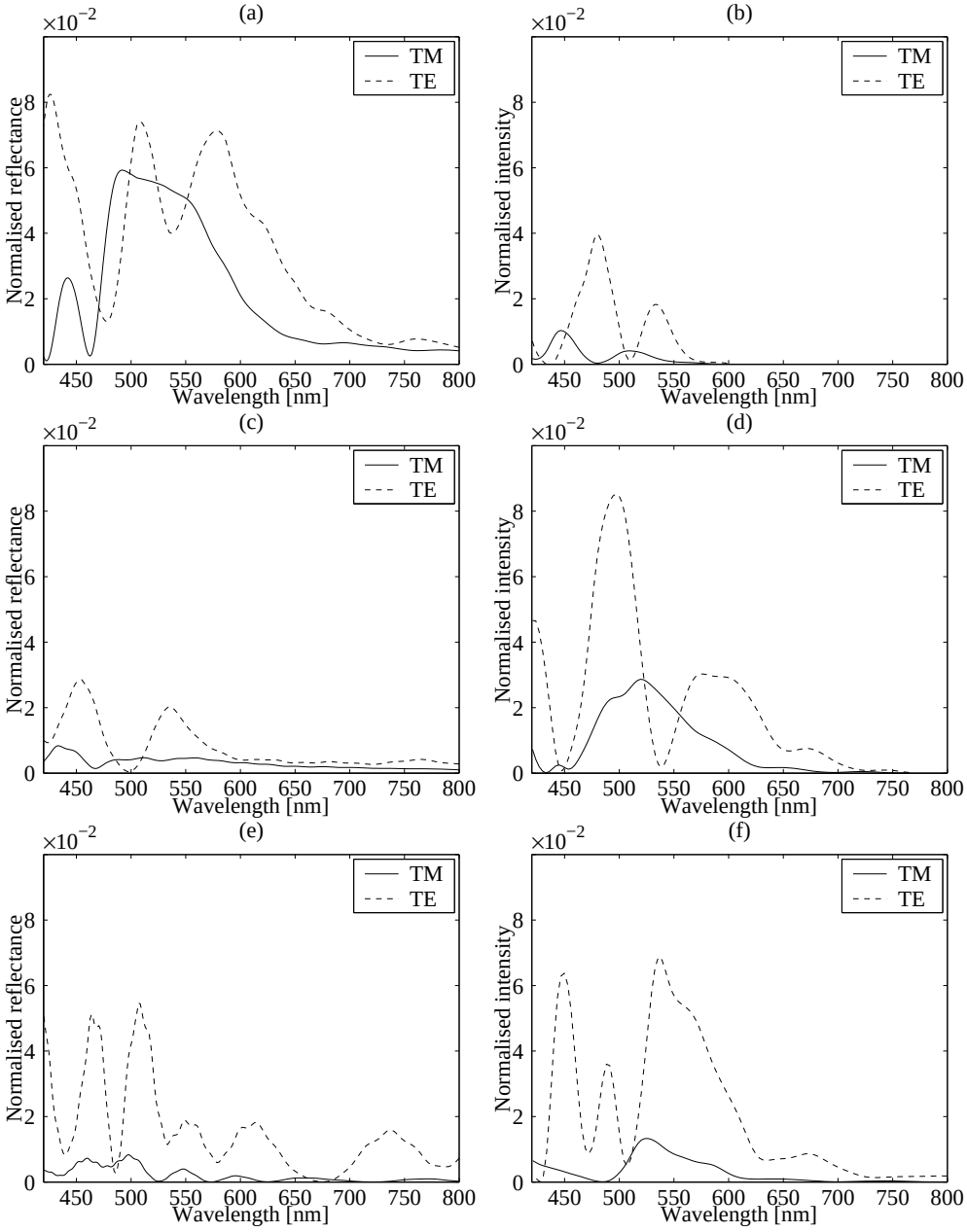

Figure 5.22: Computed spectra of the diffraction orders of a tapered lamellar volume diffractive structure with layered diffractive elements at different angles of incidence and polarisation. Plots (a), (c) and (e) show the 0^{th} diffraction order, or specular reflection, for an angle of incidence of 10°, 30° and 60°, respectively. Plots (b), (d) and (f) show the corresponding 1^{st} diffraction orders. All values are normalised to the total sampled power.

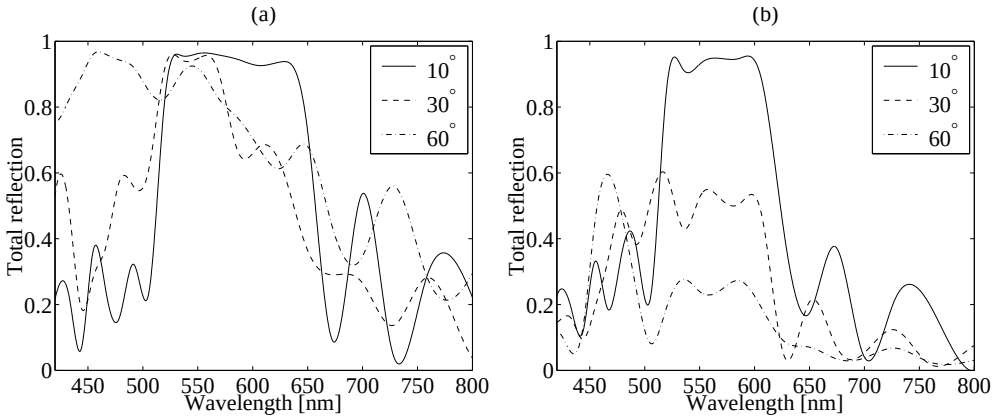

Figure 5.23: Total reflection of a straight lamellar grating at different angles of incidence and polarisation. Plot (a) shows the results for TE polarisation and (b) for TM polarisation.

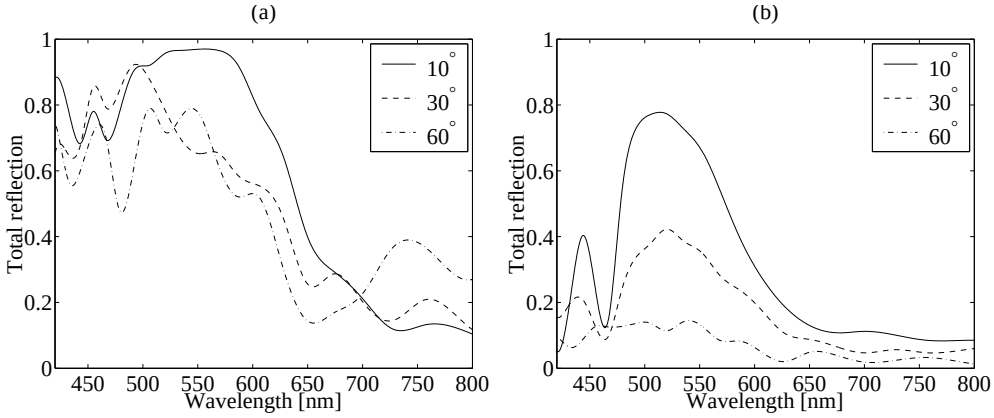

Figure 5.24: Total reflection of a tapered lamellar grating at different angles of incidence and polarisation. Plot (a) shows the results for TE polarisation and (b) for TM polarisation.

5.4 Conclusion

A novel method has been developed to compute the diffraction efficiencies of volume diffractive structures, which incorporates an FDTD core algorithm and a post-processing NFFFT algorithm. This technique is capable of generating accurate absolute values for the intensity of the scattered fields for any angle of incidence with angular and spectral resolutions of 1° and $3nm$ in the visible range of wavelengths, and models the finite volume of the interaction between electromagnetic fields and dielectrics.

With this tool a study of the reflection and diffraction properties of features occurring in the microstructure of the scales on the wings of *Morpho rhetenor* was carried out. Four structures were analysed: (a) a rectangular lattice of rectangular dielectric elements; (b) a tapered version of the above, resulting in a pine tree structure with its tips towards the incident front; (c) a centred rectangular lattice of rectangular dielectric elements; and (d) a tapered version of (c), resulting in an asymmetric pine tree structure.

For all studied structures, most of the back-scattered power is found at wavelengths shorter than $540nm$ for angles of incidence of 10° and 30° and both polarisations, with total reflections larger than 58% for 10°. The back-scattered power for the centered rectangular lattice (c) is largely concentrated in the first order of diffraction at all angles of incidence, whereas for the rectangular lattice (a) the intensity of the specular reflection is larger or comparable to that of the first order of diffraction. For both lattices, a tapering of the diffraction elements (b and d) generates qualitatively similar spectra to the non-tapered ones, but all local modulation is suppressed, and smoother and wider peaks occur.

Additionally, an analogous numerical characterisation was carried out for lamellar, volume diffractive structures composed of SiO_2 and Si_3N_4. A structure with straight diffraction elements and another with tapered ones were considered. In this case, very high diffraction efficiencies were found especially for the tapered structures, which in comparison with the straight ones also showed less locally modulated spectra and smoother peaks.

The role of the studied structures for the production of colour on the wings of *Morpho rhetenor* will be discussed in chapter 6. The discussion will include the following topics: (i) the function of individual morphological features and of the symmetry of the arrangements for the generation of the diffraction efficiencies; (ii) the agreement between diffraction properties obtained with the numerical methods presented above and band structure of the arrangements computed by expansion methods and presented in chapter 2; (iii) formulation of a two-dimensional model that accounts for the results of the experimental investigation presented in chapter 4.